

ALMA uncovers the [C II] emission and warm dust continuum in a $z = 8.31$ Lyman break galaxy

Tom J. L. C. Bakx^{1,2*}, Yoichi Tamura,¹ Takuya Hashimoto^{2,3,4}, Akio K. Inoue^{5,6},
Minju M. Lee,⁷ Ken Mawatari^{4,8}, Kazuaki Ota,⁹ Hideki Umehata,^{10,11,12}
Erik Zackrisson¹³, Bunyo Hatsukade,¹² Kotaro Kohno^{12,14}, Yuichi Matsuda,^{2,15}
Hiroshi Matsuo,^{2,15} Takashi Okamoto,¹⁶ Takatoshi Shibuya,¹⁷ Ikkoh Shimizu,²
Yoshiaki Taniguchi⁹ and Naoki Yoshida^{18,19}

Affiliations are listed at the end of the paper

Accepted 2020 February 15. Received 2020 February 10; in original form 2020 January 8

ABSTRACT

We report on the detection of the [C II] 157.7 μm emission from the Lyman break galaxy (LBG) MACS0416_Y1 at $z = 8.3113$, by using the Atacama Large Millimeter/submillimeter Array (ALMA). The luminosity ratio of [O III] 88 μm (from previous campaigns) to [C II] is 9.3 ± 2.6 , indicative of hard interstellar radiation fields and/or a low covering fraction of photodissociation regions. The emission of [C II] is cospatial to the 850 μm dust emission (90 μm rest frame, from previous campaigns), however the peak [C II] emission does not agree with the peak [O III] emission, suggesting that the lines originate from different conditions in the interstellar medium. We fail to detect continuum emission at 1.5 mm (160 μm rest frame) down to 18 μJy (3σ). This non-detection places a strong limits on the dust spectrum, considering the 137 ± 26 μJy continuum emission at 850 μm . This suggests an unusually warm dust component ($T > 80$ K, 90 per cent confidence limit), and/or a steep dust-emissivity index ($\beta_{\text{dust}} > 2$), compared to galaxy-wide dust emission found at lower redshifts (typically $T \sim 30$ –50 K, $\beta_{\text{dust}} \sim 1$ –2). If such temperatures are common, this would reduce the required dust mass and relax the dust production problem at the highest redshifts. We therefore warn against the use of only single-wavelength information to derive physical properties, recommend a more thorough examination of dust temperatures in the early Universe, and stress the need for instrumentation that probes the peak of warm dust in the Epoch of Reionization.

Key words: galaxies: formation – galaxies: high-redshift – galaxies: ISM.

1 INTRODUCTION

Forming a complete picture of star formation through cosmic time is one of the main challenges of galaxy evolution studies (Madau & Dickinson 2014). Our current understanding of star formation at high redshifts ($z > 7$) is mostly formed through rest-frame ultraviolet (UV) observations of Lyman-break galaxies (LBGs), which directly probe their stellar light (e.g. Bouwens et al. 2015; Finkelstein et al. 2015; McLeod et al. 2015; Oesch et al. 2016; Dunlop et al. 2017; Oesch et al. 2018). These recent UV observations of high-redshift LBGs suggest that most star formation is not dust-obscured, due to the short amount of cosmic time that is available for its formation, its spatial distribution across the galaxy,

and its interstellar medium (ISM, Bouwens et al. 2016; Matthee et al. 2017).

The sensitivity of the Atacama Large Millimeter/submillimeter Array (ALMA) has allowed us to detect UV-selected high-redshift galaxies at submillimetre (sub-mm) wavelengths. Recent observations have revealed far-infrared (FIR) spectral lines, such as bright doubly ionized oxygen ([O III] at 88.3 μm) lines detected from LBGs out to redshifts around 8–9 (Laporte et al. 2017; Hashimoto et al. 2018, 2019; Tamura et al. 2019). The [O III] line, however, only probes regions with strong UV radiation fields, close to hot O- and B-stars, which create high radiation pressures and ionized hydrogen (i.e. H II regions). A more complete description of the ISM requires multiple spectral line detections, each probing different phases due to their individual critical densities and temperatures. For example, the excitation energy of carbon lies slightly below the 13.6 eV required to ionize hydrogen. As such, carbon-ionizing radiation can

* E-mail: bakx@phys.nagoya-u.ac.jp

Table 1. Properties of the ALMA observations.

UT start time (YYYY-MM-DD hh:mm:ss)	Baseline lengths (m)	N_{ant}	Upper LO frequency (GHz)	Integration time (min)	PWV (mm)
2018-09-08 09:07:17	15–783	43	203.313	45.7	1.1
2018-08-30 08:50:05	15–783	43	203.313	45.6	1.1
2018-08-22 14:06:36	15–457	43	203.313	45.6	0.6
2018-11-25 07:42:49	15–1398	43	204.298	45.1	0.6
2018-11-25 05:20:34	15–1398	43	204.298	45.1	0.7
2018-11-25 06:32:22	15–1398	43	204.298	45.1	0.7

Notes: Reading from the left, the columns are: Column 1 – the starting time of the complete observation run; Column 2 – the distance between nearest and furthest ALMA antennae; Column 3 – the number of integrating antennae; Column 4 – the centre frequency of the upper frequency band, which contained the [C II] emission at ~ 204.1 GHz; Column 5 – total on-source integration time; and Column 6 – the average PWV during the observation run.

also exist within neutral hydrogen, allowing fine-structure lines of singly ionized carbon ($^2\text{P}_{3/2}$ to $^2\text{P}_{1/2}$ transition of C^+ at $157.7 \mu\text{m}$) to be emitted from neutral hydrogen regions. In the local Universe, these regions extend over larger volumes than H II regions, and combined with the prevalence of carbon, this causes the [C II]-line to be one of the most important cooling lines for the dusty ISM (e.g. Stacey 2011). The bulk of the [C II] emission line (70 per cent according to Stacey et al. 1991, 2010) is believed to originate from photodissociation regions (PDRs), and the remainder from X-ray-dominated regions, cosmic ray-dominated regions, ionized regions (H II regions; Meijerink, Spaans & Israel 2007), low-density warm gas, shocks (Appleton et al. 2013), and/or diffuse H I clouds (Madden et al. 1997).

Similarly, ALMA has observed the dust continuum emission of galaxies out to redshifts of 8.38 (Watson et al. 2015; Laporte et al. 2017; Tamura et al. 2019). The amount of dust that exists at high redshifts is fundamentally constrained by the available cosmic time needed to form it. For instance, sources at $z = 8$ have only had ~ 500 Myr to form all their dust and to enrich their ISM (Tegmark et al. 1997). This leaves only little time to form dust in the outer shells of asymptotic giant branch (AGB) stars, and to increase the dust mass by accretion of the ISM (Ferrara, Viti & Ceccarelli 2016). Dust size growth by accretion is also hindered by strong radiation fields, whose photo-ionizing effects make the dust particles become positively charged, causing them to repel each other (Ceccarelli et al. 2018). The only known dust resource would be supernovae (SNe), although dust mass estimates at high redshift require SNe to create dust at maximum efficiency (Asano et al. 2013; Gall et al. 2014; Michałowski 2015; Leńniewska & Michałowski 2019). Potentially, stars formed by pristine gas clouds, so-called Population III stars (Nozawa et al. 2014), could be an additional source of dust in the early Universe both through the more traditional SNe or during a potential red supergiant phase, however no such stars – or their tracers – have been confirmed by observations (Sobral et al. 2015, 2019; Bowler et al. 2017; Shibuya et al. 2018).

Thus, providing an adequate description of the ISM conditions, whilst also probing the dust emission properties, are important goals to our understanding of galaxy evolution in the early Universe (Dayal & Ferrara 2018). This paper reports the detection of [C II] and the stringent upper limit on the dust continuum emission at 1.5 mm of the LBG MACS0416_Y1 at redshift 8.312. We describe the target and the observations in Section 2, and present the results in Section 3. We discuss the implications of the [C II] line strength and lack of dust continuum at 1.5 mm in Section 4, where we also compare the present result against previously observed [O III] and $850 \mu\text{m}$ dust continuum. We present our conclusions in Section 5.

Throughout this paper, we assume a flat Λ -cold dark matter cosmology with the best-fitting parameters derived from the *Planck* results (Planck Collaboration XVI 2016), which are $\Omega_{\text{m}} = 0.307$, $\Omega_{\Lambda} = 0.693$, and $h = 0.693$. At $z = 8.3$, 1 arcsec corresponds to a physical distance of 4.8 kpc. We also assume the Chabrier (2003) initial mass function (IMF).

2 TARGET AND OBSERVATIONS

2.1 Target and previous observations

The target, MACS0416_Y1, was initially identified as a bright Y-dropout galaxy at $z \approx 8$ (Infante et al. 2015; Laporte et al. 2015, 2016; McLeod et al. 2015; Castellano et al. 2016; Kawamata et al. 2016; González-López et al. 2017a) lying behind the MACS J0416.1–2403 lensing cluster, one of the Hubble Frontier Fields (Lotz et al. 2017), with only a moderate magnification of $\mu = 1.43 \pm 0.04$ (Kawamata et al. 2016).

Tamura et al. (2019) report the detection of the [O III] $88 \mu\text{m}$ line emission and $850 \mu\text{m}$ dust continuum emission. The [O III] emission confirmed the spectroscopic redshift at $z = 8.3118 \pm 0.0003$. The $850 \mu\text{m}$ dust continuum is detected at $137 \pm 26 \mu\text{Jy}$, suggesting a delensed total infrared luminosity of $L_{\text{IR}} = (1.7 \pm 0.3) \times 10^{11} L_{\odot}$, assuming a modified blackbody with a dust temperature of 50 K and an emissivity index of $\beta = 1.5$ ¹.

They further report on a UV to FIR spectral energy distribution (SED) modelling, where they find a moderately metal-polluted young stellar component ($\tau_{\text{age}} = 4_{-2.3}^{+0.7}$ Myr, $Z = 0.2_{-0.18}^{+0.16}$, Z_{\odot} , $M_{*} = 2.4_{-0.1}^{+0.7} \times 10^8 M_{\odot}$, assuming the Calzetti extinction law), with a star formation rate (SFR) of around $60 M_{\odot} \text{ yr}^{-1}$. However, an analytic dust mass evolution model assuming only a single episode of star formation does not reproduce the metallicity and dust mass within these 4 Myr, suggesting a pre-existing evolved stellar component with an $M_{\text{star}} \sim 3 \times 10^9 M_{\odot}$ and an age $\tau_{\text{age}} \sim 300$ Myr, around half the age of the Universe at $z = 8.312$.

2.2 ALMA observations

The ALMA observations were initially carried out in 2018 August, September, and November as a Cycle 5 program (Program ID: 2017.1.00225.S, PI: Y. Tamura). We summarize the observations in Table 1. These observations were executed in the C43-1, -2, -3, and -4 configurations, with baseline lengths ranging from 15 to 1400 m. The precipitable water vapour (PWV) ranges from 0.6

¹These results are summarized in Table 2.

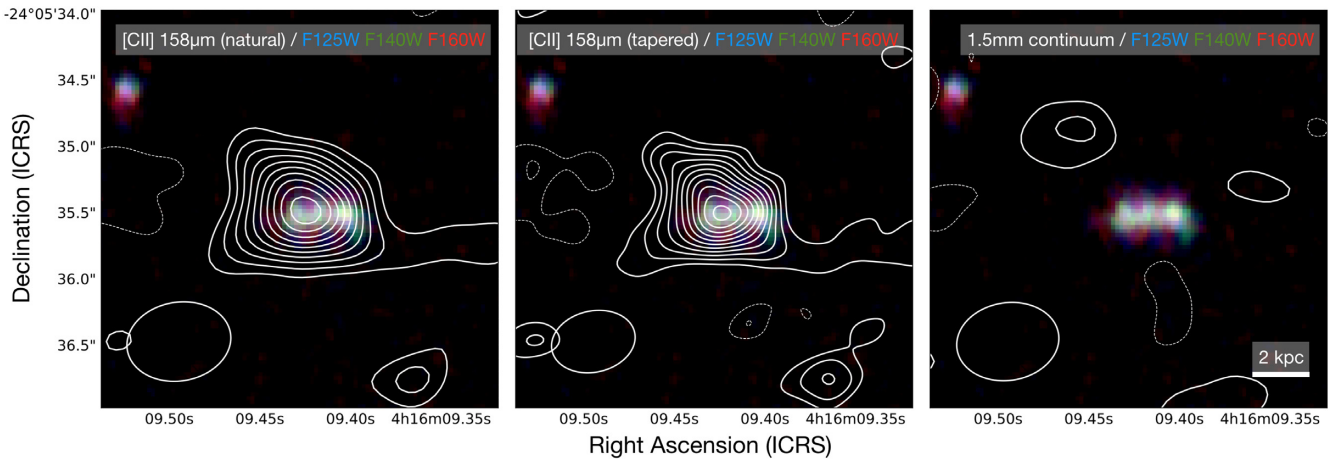


Figure 1. Left and middle: the ALMA-observed [C II] 158 μm emission of MACS0416_Y1 (-140 and $+140$ km s^{-1} around the [C II] frequency), naturally weighted (left) and tapered by a Gaussian kernel with $\text{FWHM} = 0.27$ arcsec (middle), shown as contours drawn at -2σ , 2σ , 3σ , ..., 11σ , and 12σ , respectively, where the negative contours are drawn as dashed lines. Right: the non-detected, tapered (by a Gaussian kernel with $\text{FWHM} = 0.27$ arcsec) dust continuum image at a rest-frame wavelength of 160 μm , shown as contours drawn at -2σ , 2σ , and 3σ , where negative contours are indicated with dashed lines. The bottom-left ellipse in each panel shows the beam size for the contours. All backgrounds are the *HST*/WFC3 near-infrared false-colour RGB image is composed of F160W (R), F140W (G), and F125W (B). The *Hubble* imaging suggests MACS0416_Y1 consists of eastern, central, and western components in rest-frame UV emission.

to 1.2 mm. The local oscillator frequency of the Band 5 receivers (Belitsky et al. 2018) was set from 200.5 to 204.85 GHz, in order to cover the [C II] 158 μm line at $z = 8.31$, which was expected at 204.10 GHz. In total, 272.2 min were spent effectively on-source. The phase-tracking centre was set to the UV continuum position ($\alpha_{\text{ICRS}}, \delta_{\text{ICRS}} = (04^{\text{h}}16^{\text{m}}09^{\text{s}}.4010, -24^{\circ}16'35''.470)$). Two quasars, J0348–2749 and J0453–2807, were used for complex gain calibration, and another quasar, J0522–3627, was used for bandpass calibration.

The calibration and flagging were done using the standard pipeline running on CASA (McMullin et al. 2007) version 5.4.1. A CASA task `tclean` was used to combine all visibilities into an image, both for the continuum and the [C II] emission, where the [C II]-containing channels were omitted in the continuum image. The data cube was sampled at 35 km s^{-1} (~ 23.3 MHz) to search for the [C II] line feature. We used the natural weighting on the `tclean` task to maximize the point-source flux significance. We integrate the data cube between -140 and $+140$ km s^{-1} around the [C II] frequency to generate the [C II]-integrated map², resulting in a beam size of 0.46 arcsec \times 0.64 arcsec at a position angle of -77 deg, and an rms noise of 9 mJy beam^{-1} . For the continuum map, the resulting beam size is 0.59 arcsec \times 0.78 arcsec at a position angle of -81 deg, and rms noise is 6 $\mu\text{Jy beam}^{-1}$. This -140 and $+140$ km s^{-1} velocity range was chosen because it resulted in the highest signal-to-noise ratio for the [C II] emission, and agrees with a by-eye inspection of the spectrum. Here, we calculate the rms noise from the off-source standard deviation of the maps.

3 RESULTS

3.1 Detection of the [C II] 158 μm emission

We detect the [C II] 158 μm emission at the position of MACS0416_Y1. Fig. 1 shows the *Hubble* false-colour red giant

²Integrating the data cube between larger velocity widths does not result in a significant increase in the integrated flux.

branch (RGB) image, overplotted with the contours of a naturally weighted [C II] map (left), a tapered [C II] (middle), and the [C II]-subtracted tapered continuum map (right). We create the tapered maps by convolving our naturally weighted maps using a Gaussian kernel with a full width at half-maximum (FWHM) of 0.27 arcsec. We find this FWHM size by maximizing the signal-to-noise ratio of the [C II] emission for all tapering sizes between 0.01 and 0.50 arcsec, which covers the potential angular sizes of MACS0416_Y1 expected from the [O III] emission. As noted in Tamura et al. (2019), the *Hubble* image appears to be a multi-component system, with eastern, central, and western components. They note that the 90 μm rest-frame dust continuum is centred on the eastern component, whilst the [O III] $88\mu\text{m}$ emission appears to be more centrally located.³

We calculate the central position and total apparent flux by fitting a 2D Gaussian to the naturally weighted integrated intensity image, since it has the best positional accuracy. The central position of the [C II] emission is at $\text{RA}_{\text{ICRS}}: 04^{\text{h}}16^{\text{m}}09^{\text{s}}.426$ and $\text{Dec}_{\text{ICRS}}: -24^{\circ}05'35''.470$ with a positional uncertainty of $(\sigma_{\text{RA}}, \sigma_{\text{Dec}}) = (0''.033, 0''.026)$. This position lies between the eastern and central component of MACS0416_Y1, which was also traced by the dust component in Tamura et al. (2019). Deconvolution of the [C II] emission reveals a barely resolved source size of 0.48 ± 0.14 by 0.16 ± 0.25 arcsec, at a position angle of 36 ± 36 deg, which agrees with the angular size found in the [O III] observations, whilst non-axisymmetric spur-like structure is apparent in the image. This corresponds to a physical size of 2.3 ± 0.7 by 0.8 ± 1.2 kpc at $z = 8.3$.

We use this 2D Gaussian fit to measure an apparent [C II] flux of 130.2 ± 20.4 mJy km s^{-1} on the naturally weighted image. In order to maximize the signal-to-noise ratio of the spectrum and fitted line profile, we taper the [C II] map with a 0.27 arcsec tapering size. The spectrum and a Gaussian fit to the spectrum are shown in Fig. 2, where the top panel shows the [C II] emission, and the bottom panel shows the [O III] $88\mu\text{m}$ emission from Tamura et al. (2019)

³The astrometry of the *Hubble* images are set using *Gaia* stars.

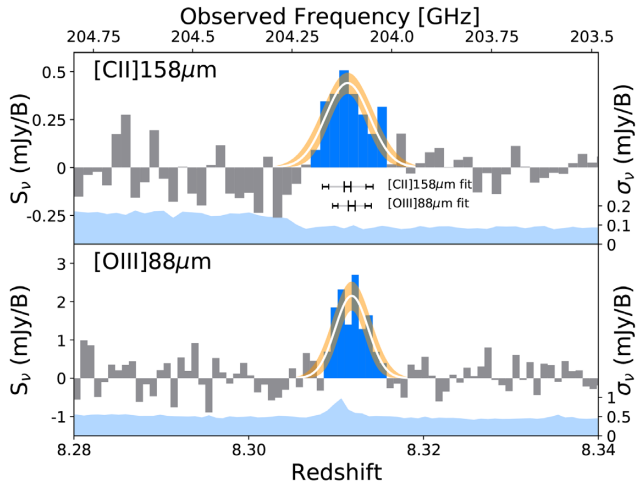


Figure 2. Top: the ALMA spectrum of MACS0416.Y1 showing the [C II] emission, binned at 35 km s^{-1} , extracted at the peak of the [C II] emission. The orange line shows the 16th–84th percentile Gaussian fit of the spectral line. The blue bins indicate those stacked to form the [C II] image. The light-blue filled line in the bottom of the panel indicates the per-bin noise level (σ_v), with the scale shown on the right-hand side. The horizontal lines underneath the [C II] line profile show the 16th–84th percentile spread of the redshifts and line widths of both [C II] and [O III] for comparison. Bottom: similar to the top figure, we show the continuum-subtracted [O III] ALMA spectrum for comparison to the [C II] emission, from Tamura et al. (2019), and extracted at the peak of the [O III] emission.

in order to compare the line profiles. The filled area at the bottom of each panel represents the uncertainty σ_v in each frequency bin, whose axes are shown on the right-hand side of the figure. The two horizontal lines below the [C II] line indicate the fitted average frequency and line width of both the [C II] and [O III] lines.

The best-fitting Gaussian profile finds a central frequency at $204.1105 \pm 0.0082 \text{ GHz}$, indicating a redshift of 8.31132 ± 0.00037 . This central frequency of the [C II] line suggests a velocity offset from the [O III] line of $\sim 15 \pm 15 \text{ km s}^{-1}$. The combined [O III] and [C II] estimated redshift is $\bar{z} = 8.31161 \pm 0.00023$, calculated using

$$\bar{z} = \sqrt{\frac{\sum_i (z_i/dz_i)^2}{\sum_i (1/dz_i)^2}}. \quad (1)$$

Here, z_i is the redshift of line i , and dz_i is the uncertainty in line i . The [C II] line width (FWHM) is $191 \pm 29 \text{ km s}^{-1}$, which is slightly larger than the line width measured for [O III] ($141 \pm 21 \text{ km s}^{-1}$), with a ΔFWHM of $50 \pm 36 \text{ km s}^{-1}$, and could be due to the difference in regions where [O III] and [C II] are predominantly emitted. We derive the line luminosity using

$$L_{\text{line}} = 1.04 \times 10^{-3} \times \left(\frac{S_{\text{line}} \Delta v}{\text{Jy km s}^{-1}} \right) \left(\frac{D_L}{\text{Mpc}} \right)^2 \left(\frac{\nu_{\text{obs}}}{\text{GHz}} \right) L_{\odot}, \quad (2)$$

from Solomon & Vanden Bout (2005), where S_{line} is the velocity-integrated flux corrected for lensing, D_L the luminosity distance, and ν_{obs} the observed line frequency. We find $(1.40 \pm 0.22) \times 10^8 L_{\odot}$ for the magnification-corrected [C II] line luminosity. We do not account for the effect of the cosmic microwave background (CMB) on the [C II] luminosity, as this is dependent on the properties of the [C II]-emitting regions. The high dust temperature we find in Section 4.3 could suggest that the regions where [C II] is emitted are also warm, significantly decreasing the CMB attenuation (Lagache, Cousin & Chatzikos 2018). Moreover, the effect of the CMB on

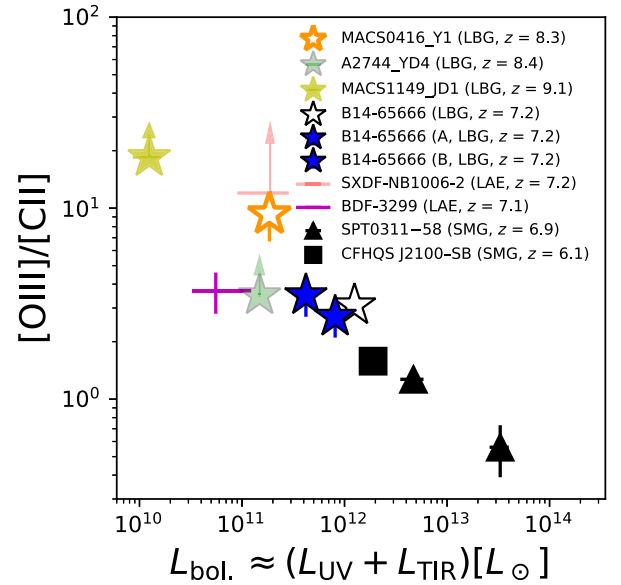


Figure 3. The [O III]-to-[C II] luminosity ratio against the total bolometric luminosity, a combination of both UV and FIR components. We find that all high-redshift LBG and LAE have a ratio larger than unity, and note a power-law trend. We describe the sources further in the text.

the [C II] emission decreases at redshifts greater than 7, suggesting the effect of the CMB is minor. Laporte et al. (2019) reported on the non-detection of [C II] from an LBG with a similar redshift ($z = 8.38$), though with only half the SFR of MACS0416.Y1, and suggested the [C II] luminosity could be underestimated by a factor of ~ 3 in the most extreme case of CMB attenuation using Lagache et al. (2018).

3.2 Upper limit of 1.5 mm dust continuum

We did not detect the dust continuum emission at 1.5 mm (200 GHz) in either the tapered or naturally weighted map, after we combine all the spectral windows, excluding the channels that contain the [C II] emission. We find a 3σ upper limit of $18 \mu\text{Jy}$ at 1.5 mm (160 μm rest frame). This is significantly lower than we expected from the $137 \pm 26 \mu\text{Jy}$ dust continuum detected at 850 μm (90 μm rest frame). In the case of a modified blackbody with a temperature of $T_{\text{dust}} = 50 \text{ K}$ and a dust emissivity of $\beta = 1.5$, we would expect a 1.5 mm flux of around $36 \mu\text{Jy}$, well above the detection limit ($\sim 6\sigma$). We more thoroughly discuss the consequences of this non-detection in Section 4.3.

4 DISCUSSION

4.1 [O III]-to-[C II] luminosity ratio

We compare the oxygen to carbon luminosity ratio to the total bolometric luminosity in Fig. 3. Here, the [O III] luminosity is from Tamura et al. (2019), who find $(1.2 \pm 0.3) \times 10^9 L_{\odot}$, resulting in a [O III]-to-[C II] luminosity ratio of 9.3 ± 2.6 , not taking CMB-dimming into account. The delensed UV luminosity of MACS0416.Y1 is $4.5 \times 10^{10} L_{\odot}$, taken from Laporte et al. (2015). The FIR luminosity is $1.7 \times 10^{11} L_{\odot}$, assuming $T_{\text{dust}} = 50 \text{ K}$ and a dust emissivity factor (β) of 1.5. While we show in Section 4.3 that this temperature is most likely higher, for fair comparison, we use

this temperature for our FIR luminosity calculation, since all other sources have assumed dust temperatures in the range of 30–60 K.

We compare our galaxy against other high-redshift LBGs, Lyman- α Emitters (LAEs) and sub-mm galaxies (SMGs) that have observations targeting both the [O III] and [C II] lines. First, we use the [C II] upper limits, combined with the FIR luminosities and [O III] of the $z = 8.38$ and 9.11 LBGs A2744_YD4 and MACS1149_JD1 (Laporte et al. 2019). We show the $z = 7.15$ LBG B14–65666 as a single luminosity-averaged source, as well as its two resolved components, from Hashimoto et al. (2019). We show the upper limit for the $z = 7.2$ LAE SXDF-NB1006-2 described in Inoue et al. (2016), and the $z = 7.1$ LAE BDF-3299 detailed in Carniani et al. (2017). Finally, we also show three $z > 6$ SMGs, the eastern and western components of SPT0311-58, and CFHQS J2100-SB, described in Marrone et al. (2018) and Walter et al. (2018) respectively, in order to compare with more dusty and star-forming galaxies. We find a high [O III]-to-[C II] ratio for MACS0416_Y1, compared to other sources with detected [C II] emission. We note that the downward trend in [O III]-to-[C II] for increasing bolometric luminosities, as mentioned in Hashimoto et al. (2019), appears consistent also for fainter sources (e.g. MACS1149_JD1).

Local dwarf galaxy studies (Cormier et al. 2015, 2019) find [O III]-to-[C II] luminosity ratios between 2 and 10 for these 0.02 to $1 Z_{\odot}$ galaxies. The low metallicity of high-redshift galaxies could thus be contributing to the high ratio, where the low metallicity allows hard radiation fields to extend over longer distances, which is necessary to produce [O III] emission. The porosity of the neutral media in these high-redshift galaxies such as MACS0416_Y1 could also play a role, since the modelling of dwarf galaxies by Cormier et al. (2019) has showed that almost all dwarf galaxies have H II regions that are directly exposed to the IGM, without shielding by a PDR. Simulations by Arata et al. (2019) suggest this porosity could be due to the shallow gravitational potential in the recently formed dark-matter haloes of high-redshift LBGs such as MACS0416_Y1. Their simulations combine cosmological zoom-in hydrodynamic simulations and radiative transfer modelling to investigate three massive galaxies (and their satellites). The total halo masses of these galaxies range between 2.4 and $70 \times 10^{10} M_{\odot}$. For reference, assuming a baryonic mass of $1 \times 10^{10} M_{\odot}$ (Tamura et al. 2019), and a baryonic-to-dark matter ratio of 5-to-27, the halo mass of MACS0416_Y1 is expected to be $\sim 6 \times 10^{10} M_{\odot}$. They showed that this shallower gravitational potential allows stellar feedback to regulate star formation, alternating between a galaxy in an infrared- and a UV-luminous phase. During each phase, the spectrum is dominated either by emission from dust-obscured star formation inside of PDRs during the infrared-luminous phase or by unobscured emission from exposed H II regions with little dust obscuration during the UV-luminous phase. Each phase is characterized by a specific [O III]-to-[C II] ratio, where the dust-obscured phase has strong [O III] emission, while the [O III]-emission becomes faint rapidly during the UV-luminous phase (Arata et al. 2020).

Pallottini et al. (2019), and previously Pallottini et al. (2017a) and Vallini et al. (2017), have modelled the formation and evolution of several LBGs in the early Universe using cosmological zoom-in simulations, accounting for ISM evolution and using radiative transfer modelling. Their 1D radiative transfer modelling showed that the efficiency of [C II] emission (luminosity over mass) drops for extreme PDR densities greater than 10^4 cm^{-3} . [C II] emission from MACS0416_Y1 could also be suppressed by the photo-electric effect of UV photons on the dust, creating free electrons that remove ionized carbon from the ISM by recombination into neutral

carbon. These findings are thus consistent with strong interstellar radiation fields, given both the relatively low [C II] emission from MACS0416_Y1, and with its warm dust temperature, as we will discuss in Section 4.3.

Simulations are, however, unable to accurately recreate the global [O III]-to-[C II] ratios seen in MACS0416_Y1 and other high-redshift galaxies. In Pallottini et al. (2019), small regions of their simulated galaxies show [O III]-to-[C II] ratios of around 10, but the global ratio of each galaxy is around 0.3. In their simulations, the most massive galaxy has a stellar mass of $4.2 \times 10^9 M_{\odot}$. They do find that [C II] is suppressed by the starburst phase of the galaxy, disrupting and photodissociating the emitting molecular clouds around star formation sites. The simulations by Katz et al. (2019) find only one galaxy with a [O III]-to-[C II] ratio greater than unity, although its SFR is less than $1 M_{\odot} \text{ yr}^{-1}$, and most galaxies with SFRs $> 10 M_{\odot} \text{ yr}^{-1}$ have ratios ranging from 0.1 down to 0.02. Their simulations are based on a suite of cosmological radiation-hydrodynamics simulations centred on LBGs that follow from adaptive-mesh cosmological simulations assuming the Planck Collaboration XVI (2016) cosmology. These cosmological simulations evolve the inhomogeneities in temperature, density, metallicity, ionization parameter, and spectral hardness. Their three most massive sources range between 4 and $42 \times 10^9 M_{\odot}$ at $z = 9$.

Harikane et al. (2019) also find a high [O III]-to-[C II] ratio for their sources, and they model the origins of this high ratio using the CLOUDY photo-ionization code (Ferland et al. 2017). Their detailed discussion of the potential causes of their high line ratio addresses (A) a higher ionization parameter, (B) a lower gas metallicity, (C) a higher gas density, (D) a lower C/O abundance ratio, (E) a lower PDR covering fraction, (F) CMB attenuation effects, (G) a spatially extended [C II] halo, and (H) inclination effects. Their modelling suggests that the high [O III]-to-[C II] ratio of their sources, and of MACS0416_Y1, can be explained by either the higher ionization parameter (A) or the lower PDR covering fraction (E). Similarly, a combination of a higher gas density (C), a lower C/O abundance ratio (D), and the effect of the CMB (F) are adequate for explaining the high ratio of MACS0416_Y1. Their CLOUDY modelling is able to exclude the low metallicity (B) as an explanation for the high ratio of their sources and of MACS0416_Y1. The [C II] flux of MACS0416_Y1 does not appear to increase for larger apertures, disqualifying missed [C II] emission due to a spatially extended [C II] halo (G) around MACS0416_Y1. Finally, the inclination effects (H) can be disqualified since this should affect both the [C II] and [O III] lines of MACS0416_Y1 to a similar extent, especially since the line profiles (Fig. 2) suggest they lie in the same plane.

4.2 [C II] line luminosity, profile, and geometry

4.2.1 Line luminosity

We plot the [C II] line luminosity against the integrated (UV+IR) SFR in Fig. 4, where we take the SFR for MACS0416_Y1 from Tamura et al. (2019). They assume a Chabrier IMF to calculate the total SFR (Chabrier 2003) using UV-to-FIR spectral modelling tool PANHIT⁴ (Mawatari et al. 2016, Hashimoto et al. 2018, and Mawatari et al. 2020). We compare MACS0416_Y1 against high-redshift observations, simulations from Pallottini et al. (2019) and two [C II]-SFR_{FIR} scaling relations from de Looze et al. (2014)

⁴Panchromatic Analysis for Nature of High- z galaxies Tool (PANHIT), <http://www.icrr.u-tokyo.ac.jp/mawatari/PANHIT/PANHIT.html>

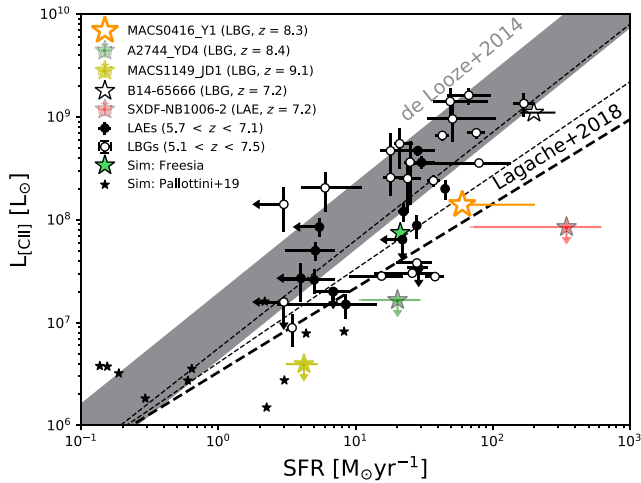


Figure 4. The [C II] line luminosity compared to the total (UV+IR) SFR for MACS0416_Y1, high-redshift sources, simulations (Pallottini et al. (2019), separately indicating the brightest galaxy: Freesia) and the scaling relations from de Looze et al. (2014) and Lagache et al. (2018). We show the Lagache et al. (2018) scaling relations for $z = 8.3$ (bold dashed line), and $z = 5$ and 7 (thin dashed lines). We find a slight [C II] deficit among the highest redshift sources, when compared to other LBGs and the relation from de Looze et al. (2014). We find good agreement with the scaling relation from Lagache et al. (2018).

and Lagache et al. (2018). We show the [C II] upper limits and SFR estimates of the $z = 8.38$ and 9.11 LBGs A2744_YD4 and MACS1149_JD1 from Laporte et al. (2019), where the SFR of the $z = 8.38$ galaxy is calculated by MAGPHYS and of the $z = 9.11$ is calculated using PANHIT model (Hashimoto et al. 2018). We show the $z = 7.15$ LBG B14–65666 from Hashimoto et al. (2019), where the SFR is calculated using the same SED fitting model as MACS0416_Y1. We also show the upper limit for the $z = 7.2$ LAE SXDF-NB1006-2 described in Inoue et al. (2016), and use the SFR calculated using a Chabrier IMF, taken from Harikane et al. (2019). The high-redshift observations refer to a combination of $5.7 < z < 7.1$ LAEs from Bradač et al. (2017), Carniani et al. (2017, 2018), Kanekar et al. (2013), Matthee et al. (2017), Ota et al. (2014), and Smit et al. (2018) and $5.1 < z < 7.5$ LBGs from Barisic et al. (2017); Capak et al. (2015), Jones et al. (2017), Knudsen et al. (2016), Schaerer et al. (2015), and Willott et al. (2015). We compare against simulations by Pallottini et al. (2019), highlighting its most massive galaxy (Freesia, $M_{\text{star}} = 4.2 \times 10^9 M_{\odot}$, Pallottini et al. 2017a, b). The de Looze et al. (2014) scaling relation is based on the SFR derived from UV and mid-IR observations of both low-metallicity local dwarf galaxies. The Lagache et al. (2018) scaling relation is based on the combination of a semi-analytical model (G.A.S., Cousin, Guillard & Lehnert 2019) and the CLOUDY photo-ionization code (Ferland et al. 2017), where they assume PDRs are the dominant region where the [C II] is emitted. Their redshift-dependent [C II] scaling relation agrees with recently observed, high-redshift observations of UV- and blindly selected sources, although the scaling relation has difficulty in reproducing the [C II] emission from high- z SMGs. Here, we show the scaling relation for $z = 8.3$ (bold dashed line) and for $z = 5-7$ (thin dashed lines). For lower redshifts, this line steepens and rises.

The [C II] emission of our $z = 8.31$ LBG, MACS0416_Y1, appears fainter than predicted by the relation of de Looze et al. (2014). This is also seen for the other $z > 8$ galaxies, which all

appear to lie below the scaling relation from de Looze et al. (2014). The high-redshift LAEs and the simulated LBGs in Pallottini et al. (2019) also exhibit a deficit in the [C II] emission, while this is not seen for actual observations of $z < 8$ LBGs in general. The scaling relation by Lagache et al. (2018) agrees with our [C II] luminosity, and appears to agree most of the $z > 8$ LBGs and the LAEs. The relationship seems to underpredict the [C II] luminosity of the $5.1 < z < 7.5$ LBGs (black-and-white circles), as well as for $z = 7.2$ LBG B14-65666 (black star, Hashimoto et al. 2019).

The LAEs typically lie below the LBGs in Fig. 4, except for the $z > 8$ LBGs, such as MACS0416_Y1. Lyman- α emission originates in hard radiation fields, which deplete the neutral medium, and therefore decrease the [C II] luminosity (Cormier et al. 2015, 2019). For increasing redshift, however, it becomes more difficult to detect this Ly- α emission since the Universe is not yet ionized at those redshifts ($z_{\text{re}} = 7.7 \pm 0.8$, Planck Collaboration VI 2018), and at $z = 8.3$, MACS0416_Y1 is likely located in a mostly neutral intergalactic medium. $z > 8$ LBGs such as MACS0416_Y1 could thus more closely resemble lower redshift LAEs than LBGs.

The position of MACS0416_Y1, compared to the de Looze et al. (2014) scaling relation, agrees with the simulations by Pallottini et al. (2019). Their spatially resolved simulations indicate that the larger molecular clouds shield the [C II] efficiently, decreasing the [C II] emission of these regions to around an order of magnitude below the expected behaviour from de Looze et al. (2014). Instead, the Lagache et al. (2018) scaling relation seems to agree with these simulations as well as MACS0416_Y1, and also reproduces the flatter slope in the [C II]–SFR scaling relation seen in these simulations. The lack of [C II] emission seen for the $z = 8.38$ and 9.11 LBGs (Laporte et al. 2019) could be due to the large scatter on the scaling relations (~ 0.5 dex), or potentially due to inclination effects, where the added velocity width of an edge-on galaxy pushes the line peak below the detection limit (e.g. Kohandel et al. 2019). CLOUDY modelling by Ferrara et al. (2019) attributes the lack of [C II] luminosity compared to the local de Looze et al. (2014) scaling relation for MACS0416_Y1 and other $z > 8$ galaxies to three factors, namely (i) bursty star formation, causing high SFRs for their [C II] luminosity, (ii) low metallicity, and (iii) low gas density. Only the first factor, bursty star formation, applies to MACS0416_Y1, as both its SFR and gas density are too high to cause a decrease in [C II] luminosity. Bursty episodes of star formation are also seen in modelling by Arata et al. (2019), and this burstiness produces a similar scatter on the [C II]–SFR diagram as predicted by Ferrara et al. (2019) and Arata et al. (2020).

4.2.2 Velocity profile

Observationally, one can classify star-forming galaxies into either rotation- or dispersion-dominated systems by their kinematic profile. Typically, rotation-dominated galaxies have $\Delta v/2\sigma_{\text{tot}} > 0.4$ (Förster Schreiber et al. 2009). Here, Δv is the peak-to-peak velocity across the source, and σ_{tot} is the line standard deviation. The high signal-to-noise ratio of our [C II] emission allows us to look for a velocity gradient in the [C II] emission. Fig. 5 shows the velocity component of MACS0416_Y1, created with the `immo` task within CASA. The peak-to-peak velocity is around $100-120 \text{ km s}^{-1}$. This results in $\Delta v/2\sigma_{\text{tot}} \approx 0.6-0.7$, suggesting a rotationally dominated disc, similar to what was seen by Smit et al. (2018). They reported on two LBGs at $z \sim 6.8$, with masses around $1.4-1.7 \times 10^9 M_{\odot}$.

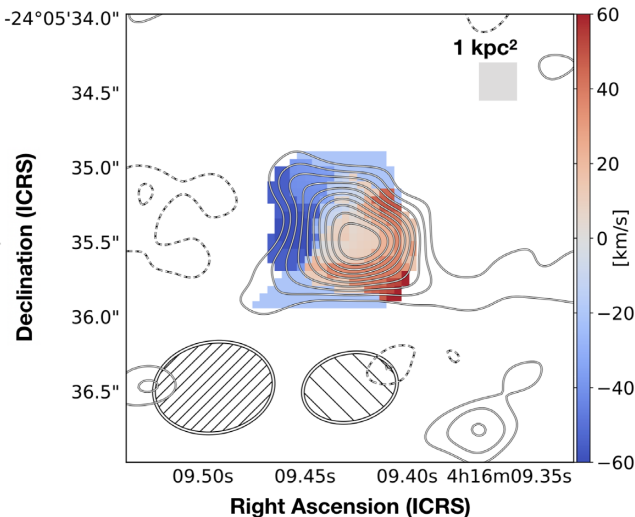


Figure 5. The velocity component (first moment map) of the [C II] emission of MACS0416_Y1 in the image plane shows a velocity gradient Δv of around 100 to 120 km s⁻¹. The foreground contours show the [C II] emission drawn at $-2\sigma, 2\sigma, 3\sigma, \dots, 11\sigma,$ and 12σ , where the negative contours are indicated with dashed lines. The leftmost ellipse in the bottom of the figure indicates the background beam size, and the more central ellipse indicates the beam size of the foreground contours. In the top right, we indicate the size of one square kiloparsec in the source plane. If we interpret this velocity gradient as a rotation, this suggests that MACS0416_Y1 is a rotation-dominated system, rotating around the central [C II] position. Other possibilities include galactic inflows or outflows, and a merging scenario.

From this, we can calculate the dynamical mass, M_{dyn} , if we assume the virial theorem,

$$M_{\text{dyn}} = C \frac{r_{1/2} \sigma_{\text{line}}^2}{G}. \quad (3)$$

Here, $r_{1/2}$ is the half-light radius, G is the gravitational constant, and the factor C depends on various effects, such as line-of-sight projection, galaxy mass, and the contributions from rotational and random motions. This value ranges from 2.25 for an average value of known galactic mass distribution models (Binney & Tremaine 2008) to 6.7 for dispersion-dominated systems (Förster Schreiber et al. 2009). Given that MACS0416_Y1 is rotationally dominated, we take C to be 3.4 from Erb et al. (2006), which is derived for an average inclination angle of the disc, assuming a rotating system. Since our system is rotationally dominated, we take the deconvolved major axis as the half-light radius, equalling 1.15 ± 0.35 kpc.

We find a dynamical mass of $(1.2 \pm 0.4) \times 10^{10} M_{\odot}$, although we note that the uncertainty in C is not accounted for, and could vary by a factor of 2. The UV-to-FIR modelling in Tamura et al. (2019) found a young stellar mass of $\sim 2.4^{+0.5}_{-0.3} \times 10^8 M_{\odot}$ (varying slightly from model to model), and their analytic galaxy evolution model, where dust mass evolution is taken into account, predicts an older stellar component with a mass of $M_{\text{star}} \sim 3 \times 10^9 M_{\odot}$ (Asano et al. 2013). This places the stellar-to-dynamical ratio around 25 per cent, which is similar to Smit et al. (2018), and in line with the star-forming galaxies at $z \approx 2-3$ (Erb et al. 2006; Gnerucci et al. 2011). The value is an order-of-magnitude larger than seen for a $z = 7.15$ LBG (Hashimoto et al. 2019), although they only take the mass of the young stellar component into account. The galaxy evolution model of Tamura et al. (2019) further predicts a gas mass of $\sim 1 \times 10^{10} M_{\odot}$, which is similar to the value we find with the kinematics, suggesting the enclosed mass is baryon-dominated.

Potentially, this apparent rotation could also be explained by other phenomena. For instance, the velocity gradient could also be a bipolar outflow. This velocity gradient is in the same direction as the spur-like feature seen in the [C II] emission, although it is along the major axis of the UV image of the LBG. The distance of the peak positive velocity relative to the centre of the [C II] emission is 3 kpc, not accounting for projection and lensing magnification effects. There, the typical escape velocity for a halo with a mass of $\sim 1 \times 10^{10} M_{\odot}$ is around 85 km s⁻¹, which is of the same order as the peak positive velocity (~ 60 km s⁻¹) enabling the possibility that the spur-like profile is a galactic outflow. This would agree with the feedback/outflow phase seen in simulations by Arata et al. (2019). Gas column densities in the outflowing regions of the simulated galaxies by Arata et al. (2019) range between 1 and 100 $M_{\odot} \text{pc}^{-2}$. Our current beamwidth does not allow us to resolve the individual outflowing regions, however an outflow moving at 60 km s⁻¹ stretching over 1 sq kpc (indicated in Fig. 5) with a gas column density of 10 M_{\odot} (typical in the range from Arata et al. 2019) would result an outflow-rate of 60 $M_{\odot} \text{yr}^{-1}$. The outflow rate could thus equal or surpass the SFR (i.e. a mass-loading factor of around or greater than unity), impacting the galaxy evolution at high redshift. There also exists observational indications for outflows at slightly lower redshifts, $z \sim 4-7$, which could support the outflow hypothesis for MACS0416_Y1. [C II]-identified outflows have been suggested for $z = 5-7$ star-forming galaxies (SFR between 10 and 70 $M_{\odot} \text{yr}^{-1}$) in Fujimoto et al. (2019) by stacking the ALMA data of 18 galaxies. Similarly, among a sample of 118 normal star-forming galaxies at $4 < z < 6$, Ginolfi et al. (2020) report high-velocity tails (~ 500 km s⁻¹) in the stacked [C II] emission, observed by ALMA. These velocity tails are indicative of outflows, and appear more prominent among more actively star-forming galaxies ($> 25 M_{\odot} \text{yr}^{-1}$). This correlation confirms the star formation-driven nature of the outflows, however these [C II]-line velocities are much larger than the ~ 60 km s⁻¹ seen in MACS0416_Y1.

The reverse scenario, the inflow of gas, could similarly explain the observed phenomena. However, at $z = 8.31$, the pristine intergalactic medium is unlikely to be enriched enough to be bright in [C II] emission. Instead, it could be previously ejected gas falling back in on to the galaxy, previously enriched by the older stellar population (Tamura et al. 2019). This would place the galaxy at the end of the feedback/outflow phase seen in the simulations by Arata et al. (2019), and would suggest an imminent starburst phase. In this scenario, the free-fall time-scale would be around 9 Myr, assuming a total enclosed mass of $1 \times 10^{10} M_{\odot}$, and a radius of 2.3 kpc. The high dust temperature (see Section 4.3) does seem to contradict a late stage feedback/outflow scenario, since the warm dust (> 80 K) in the centre of the galaxy is expected to cool down efficiently, exacerbating the problem of the high dust temperature seen for MACS0416_Y1.

A final possibility is that this galaxy actually consists of multiple merging sources, smoothed over the beam size. This does agree with the multicomponent nature seen in the rest-frame UV *Hubble* imaging. Currently, the most likely scenario seems a rotation-dominated disc given the observed velocity gradient, although future high-resolution observations of MACS0416_Y1, or a stacked spectrum of multiple $z > 8$ LBGs, are required to confirm any of the above scenarios.

4.2.3 [C II] geometry

The left-hand panel of Fig. 6 shows the [C II] emission as contours on top of the previously observed [O III] emission image. There

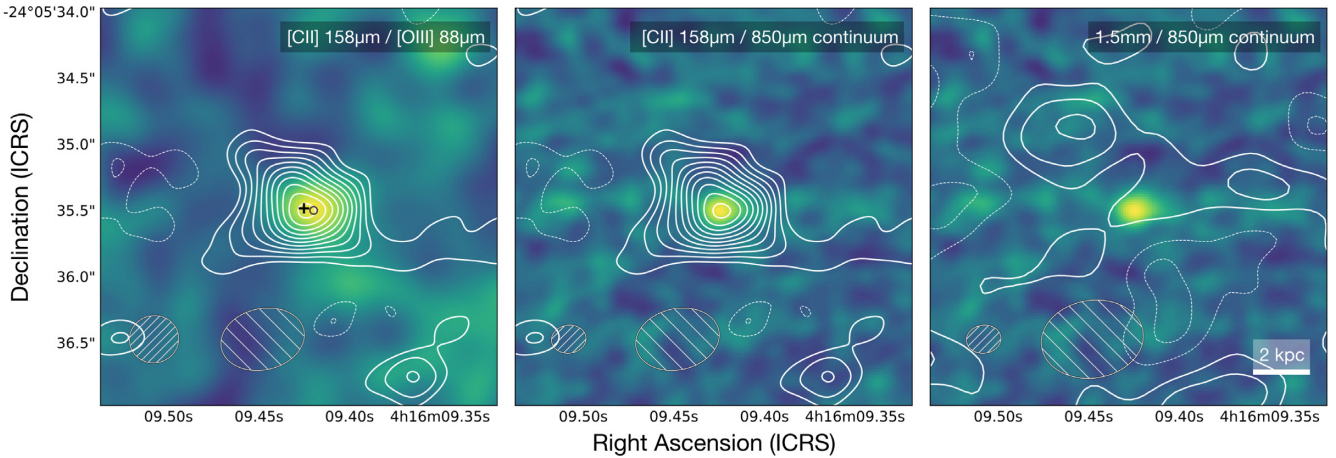


Figure 6. Left and middle: the [C II] contours (drawn at -2σ , 2σ , 3σ , ... 11σ , where negative contours are indicated with dashed lines) are shown on top of the [O III] and 850 μm dust continuum emission images from Tamura et al. (2019), respectively. There appears to be a positional offset between the [C II] and [O III] position, agreeing with the eastern and centre components seen in the *Hubble* images, and indicated with a plus ([C II]) and circle ([O III]). The [C II] and 850 μm dust continuum emission profiles appear to be aligned, suggesting the origin of the radiation to be in the same location. Right: the 1.5 mm dust continuum contours are drawn at more levels for extra contrast, namely -2σ , -1σ , 1σ , 2σ , and 3σ , with negative contours indicated with dashed lines, and are shown on top of the continuum emission image at 850 μm from Tamura et al. (2019). No significant emission can be seen, which places a strong upper limit on the LBGs spectrum. We discuss the relevance of this in Section 4.3. The leftmost ellipse indicates the background beam size, and the more centrally located ellipse indicates the beam size of the contours.

appears to be a slight angular offset between the [C II] and [O III] emission, which could be due to the different place of origin. [C II] predominantly emerges from PDRs, whereas [O III] only exists within H II regions.

The exact position of [O III] from Tamura et al. (2019) is $(\alpha_{\text{ICRS}}, \delta_{\text{ICRS}}) = (04^{\text{h}}16^{\text{m}}09^{\text{s}}.420, -24^{\circ}05'35''.495)$, which is 95 mas offset from the [C II] emission, where both positions are measured by fitting a 2D Gaussian shape to the line emission. The systematic positional uncertainty in the astrometry for the [C II] and [O III] emission are around 20 and 6 mas, respectively. Combined with the positional uncertainties, this is a 2σ offset, and if real, would equal a projected distance of ~ 450 pc.

Similar angular offsets have been seen both in previous observations and in simulations. Carniani et al. (2017) find more extended [C II] emission, and a ~ 1 kpc offset between the brightest [C II] and [O III] clump, for a normal star-forming galaxy at $z = 7.1$. They find both the [C II] and [O III] emission are significantly offset (~ 3 – 5 kpc) from the main rest-frame UV emission, find three [O III] emission clumps with distinct relative velocities, and find the [C II] emission consisting of a clumpy and an extended component. Recent simulations by Katz et al. (2019) show the positional distribution of infrared lines over a galaxy, and predict an offset between [C II] and [O III] due to their different clouds of origin (Carilli & Walter 2013) at very high redshift ($z \sim 10$). In one execution of their simulation, they find angular offsets between the peaks of [C II] and [O III] emission of 0.5–1 kpc. Similarly, recent work by Pallottini et al. (2019) sees a positional (~ 1 kpc) and spectral (~ 100 km s^{-1}) offset between [C II] and [O III] emission in their simulated galaxies. They show that this is both because [C II] and [O III] originate from different environments in the ISM, and because a more extended, but inhomogeneous, distribution of [C II] emission can shift the peak flux away from the peak [O III] emission.

While we can expect a difference in velocity and velocity width of the [C II] and [O III] lines, the error bars in Fig. 2 show that the spectral lines do not appear to differ significantly. Quantitatively, the peak of each line is offset by 15 ± 15 km s^{-1} , and the velocity width between the lines differs by 50 ± 36 km s^{-1} .

The middle image of Fig. 6 suggests the [C II] emission originates in the same region as 850 μm continuum emission. This is similar to what was seen in Pallottini et al. (2019), and in agreement with the statistical relations seen both for high-redshift sources (e.g. Smit et al. 2018) and sub-mm sources in general (e.g. de Looze et al. 2014).

4.3 The lack of 1.5 mm continuum emission

We had expected to detect the 160 μm rest-frame emission from MACS0416_Y1, given the assumed spectrum from Tamura et al. (2019). Here, we analyse the significance of the non-detection, and provide explanations for the lack of continuum emission.

4.3.1 Fitting a spectrum

The basic theoretical description of a sub-mm spectrum of a dusty source is determined exclusively by the dust temperature and the dust-emissivity index, β (e.g. Dunne & Eales 2001). At higher redshifts, the CMB becomes an important component in the heating of the dust. Throughout this analysis, we use the adjustment equations from da Cunha et al. (2013) to include the effects of CMB, both accounting for the CMB dust heating and the contrast of the emission against the CMB. This allows us to discuss CMB-corrected dust temperatures and observed flux densities, as though the source were affected by the CMB at redshift 0 (i.e. $T_{z=0}$, with $T_{\text{CMB}} = 2.73$ K).

In Fig. 7, we show the results from fitting a single-temperature modified blackbody with different β for a range of possible temperatures. We fit these modified blackbodies by adjusting the normalization, A , such that we minimize the chi-squared, χ^2 . Our data are the single 850 μm (rest-frame 90 μm) continuum detection and two continuum upper limits at 1.1 and 1.5 mm (rest-frame 120 and 160 μm). The 120 μm non-detection is from a Band 6 ALMA project (PI: F. Bauer, 2013.1.00999.S) aiming to constrain the photometry of sources behind strong-lensing clusters (González-

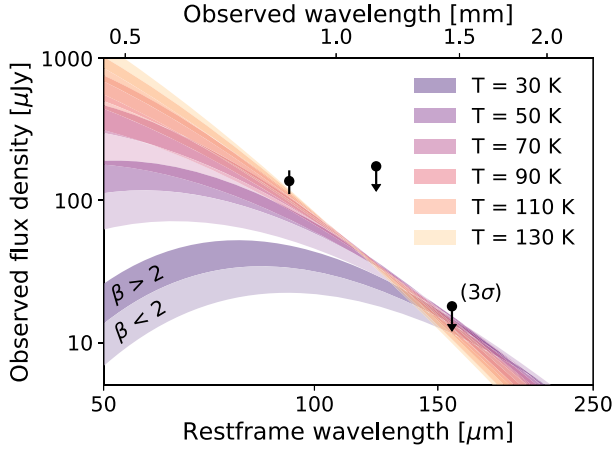


Figure 7. We fit modified blackbodies with various fixed temperatures to the single continuum data point, and two upper limits (shown at 3σ), with β varying from 1.5 to 2.5. The lighter fills show the modified blackbody spectra with $1.5 < \beta < 2.0$, while the darker fills show the spectra with $2.0 < \beta < 2.5$. Our non-detection of continuum at 1.5 mm (rest-frame $\sim 160 \mu\text{m}$) provides a stringent lower limit on the dust temperature. We account for both CMB-heating and CMB-contrast using the equations of da Cunha et al. (2013), in order to discuss the CMB-corrected dust temperature ($T_{z=0}$) in the observed flux density.

López et al. 2017b). The 160 μm non-detection, with an rms noise down to 6 μJy , provides a significant upper bound on the dust parameter space probed by these observations. The upper limits are taken into account as discussed in Sawicki (2012), where an adjustment on the χ^2 is demonstrated to be

$$\delta\chi^2 = -2 \ln \int_{-\infty}^{\sigma_j + S_j} \exp \left[-\frac{1}{2} \left(\frac{f - AS_{\text{model}}}{\sigma_j} \right)^2 \right] df. \quad (4)$$

In this equation, we calculate χ^2 for over all non-detections j , and integrate the Gaussian flux distribution along flux, f , up to the detection criterion, which is set to the measured standard deviation (σ_j) plus the value observed at the central position (S_j). The adjustment to the χ^2 measures the probability that the model-predicted value (AS_{model}) is scattered below the detection limit due to random fluctuations.

The fitted spectra in Fig. 7 appear to favour higher temperatures and β -values, and the 1.5 mm continuum upper limit seems to exclude any temperature less than ~ 90 K for $\beta < 2$, although for increasing $\beta > 2$, slightly cooler temperatures are possible.

Table 3 quantifies the results, by showing the χ^2 value for different fixed temperature and β values, which we use as a measure of the fitting quality. Given the degeneracy between β and temperature, we cannot fit these values directly, as this fit results in physically unrealistic temperatures (e.g. $T_{\text{dust}} > 200$ K or $\beta > 4$). Instead, we find the 90 per cent confidence limit from the χ^2 value. From Avni (1976), we use that a 90 per cent confidence limit can be placed on a single varied parameter if the fitting of a model results in a $\Delta\chi^2$ value of 2.7. For each value of β , we calculate the 90 per cent lower limit for the dust temperature, which we show in the final row of the table. We linearly interpolate the temperature for the two nearest χ^2 values to 2.7 for each value of β . This calculates the 90 per cent lower limit on the temperature, luminosity and dust mass. The resulting χ^2 from the two constraining data points (at 850 and 1500 μm) agree with the visual analysis of Fig. 7, suggesting dust temperatures > 80 K for $\beta = 2$. We estimate the dust mass

Table 2. Line and continuum properties of MACS0416_Y1.

Parameter	Value
Our observations	
$S_{1.5\text{mm}}^{\ddagger}$	$< 18 \mu\text{Jy} (3\sigma)$
$\text{FWHM}_{1.5\text{mm}}^{\ddagger}$	$0.59 \text{ arcsec} \times 0.78 \text{ arcsec}$
$F_{[\text{C II}]}^{\ddagger}$	$130.2 \pm 20.4 \text{ mJy km s}^{-1}$
Δv	$191 \pm 29 \text{ km s}^{-1}$
$z_{[\text{C II}]}$	8.31132 ± 0.00037
$L_{[\text{C II}]}$	$(1.40 \pm 0.22) \times 10^8 L_{\odot}$
Previous ALMA observations [†]	
$S_{850\mu\text{m}}^{\ddagger}$	$137 \pm 26 \mu\text{Jy}$
$\text{FWHM}_{850\mu\text{m}}^{\ddagger}$	$0.36 \text{ arcsec} \times 0.10 \text{ arcsec}$
$S_{1140\mu\text{m}}^{\ddagger}$	$< 116 (2\sigma) \mu\text{Jy}$
$F_{[\text{O III}]}^{\ddagger}$	$660 \pm 160 \text{ mJy km s}^{-1}$
Δv	$141 \pm 21 \text{ km s}^{-1}$
$z_{[\text{O III}]}$	8.3118 ± 0.0003
$L_{[\text{O III}]}$	$(1.2 \pm 0.3) \times 10^9 L_{\odot}$

Notes: [†] Values are from Tamura et al. (2019).

[‡] Not corrected for lensing magnification

according to equation (1) in Magdis et al. (2011),

$$M_{\text{dust}} = \frac{S_{\nu} D_L^2}{(1+z)\kappa_{\text{rest}} B_{\nu}(\lambda_{\text{rest}}, T_d)}. \quad (5)$$

Here, S_{ν} is the observed flux density, D_L is the luminosity distance, z is the spectroscopic redshift, κ_{rest} is the rest-frame dust mass absorption coefficient at the observed wavelength and $B_{\nu}(\lambda_{\text{rest}}, T_d)$ is the blackbody radiation expected for a T_d [K] source at λ_{rest} . The dust emissivity is assumed such that $\kappa_{\text{rest}} = \kappa_{850\mu\text{m}} (\nu / \nu_0)^{\beta}$, where $\nu_0 = 353$ GHz, and $\kappa_{850\mu\text{m}} = 0.15 \text{ m}^2 \text{ kg}^{-1}$ (Draine 2003). The black-body emission is corrected for its contrast against the CMB, and the dust temperature is corrected for the heating by the CMB.

We note that the dust temperature has a significant impact on the dust mass. The magnified dust mass estimate in Tamura et al. (2019) from Band 7 ALMA observations is $5.6 \times 10^6 M_{\odot}$. This dust mass is very temperature-dependent, where even the lower limit on the dust temperature suggests magnified dust masses of around $0.5 \times 10^6 M_{\odot}$, a ten-fold decrease in dust mass from the estimate in Tamura et al. (2019). The effect of the dust emissivity coefficient, β , on the dust mass is less strong, changing the dust mass by ~ 50 per cent. We discuss the consequences of the variance in dust mass with dust temperature below.

4.3.2 Comparison of [C II] emission to dust temperature

We show a modified version of the [C II] to FIR luminosity ratio as a function of temperature for MACS0416_Y1 in Fig. 8. Since the luminosity is very temperature-dependent, we use the temperature-corrected luminosity in order to compare the [C II] to FIR luminosity ratio for MACS0416_Y1 over a large range of temperatures (20–100 K, Malhotra et al. 1997; Gullberg et al. 2015). We calculate this temperature-corrected ratio by multiplying the [C II] to FIR luminosity ratio by the temperature normalized at 40 K to the fourth power.⁵

⁵ We choose 40 K, similar to Gullberg et al. (2015), since this is a typical dust temperature in the local Universe, which ensures that the temperature-corrected luminosity ratios are of the same order as non-corrected ratios.

Table 3. The fitting parameters of the tested single-temperature spectrum fits.

$\beta = 1.5$				$\beta = 2.0$				$\beta = 2.5$			
$T_{z=0}$ (K)	μIR luminosity ($10^{11} L_{\odot}$)	χ^2 –	$\mu\text{M}_{\text{dust}}$ ($10^6 M_{\odot}$)	$T_{z=0}$ (K)	μIR luminosity ($10^{11} L_{\odot}$)	χ^2 –	$\mu\text{M}_{\text{dust}}$ ($10^6 M_{\odot}$)	$T_{z=0}$ (K)	μIR luminosity ($10^{11} L_{\odot}$)	χ^2 –	$\mu\text{M}_{\text{dust}}$ ($10^6 M_{\odot}$)
30	0.31	18.9	11	–	0.49	15.8	5.1	–	0.76	12.2	2.28
50	1.34	10.3	3.0	–	2.21	6.79	1.2	–	3.56	3.88	0.47
70	4.53	6.15	1.6	–	8.11	3.40	0.6	–	14.4	1.51	0.22
90	12.2	4.15	1.1	–	23.8	2.00	0.4	–	46.4	0.64	0.14
110	28.5	3.07	0.8	–	59.8	1.30	0.3	–	126.8	0.23	0.10
130	59.2	2.42	0.7	–	133.4	0.90	0.2	–	310.8	0.019	0.085
121	46.0	2.7 (90%)	0.74	80	15.9	2.7 (90%)	0.5	60	8.95	2.7 (90%)	0.35

Notes: for each value of β , reading from the left, the columns are: Column 1 – CMB-corrected dust temperature; Column 2 – FIR luminosity, not corrected for magnification, μ ; Column 3 – χ^2 value, measuring quality of fit; and Column 4 – dust mass, not corrected for magnification. The bottom row (bold text) shows the 90 per cent lower limit on the dust temperature, FIR luminosity, and dust mass for each β , found by interpolating the χ^2 to a value of 2.7 (Avni 1976).

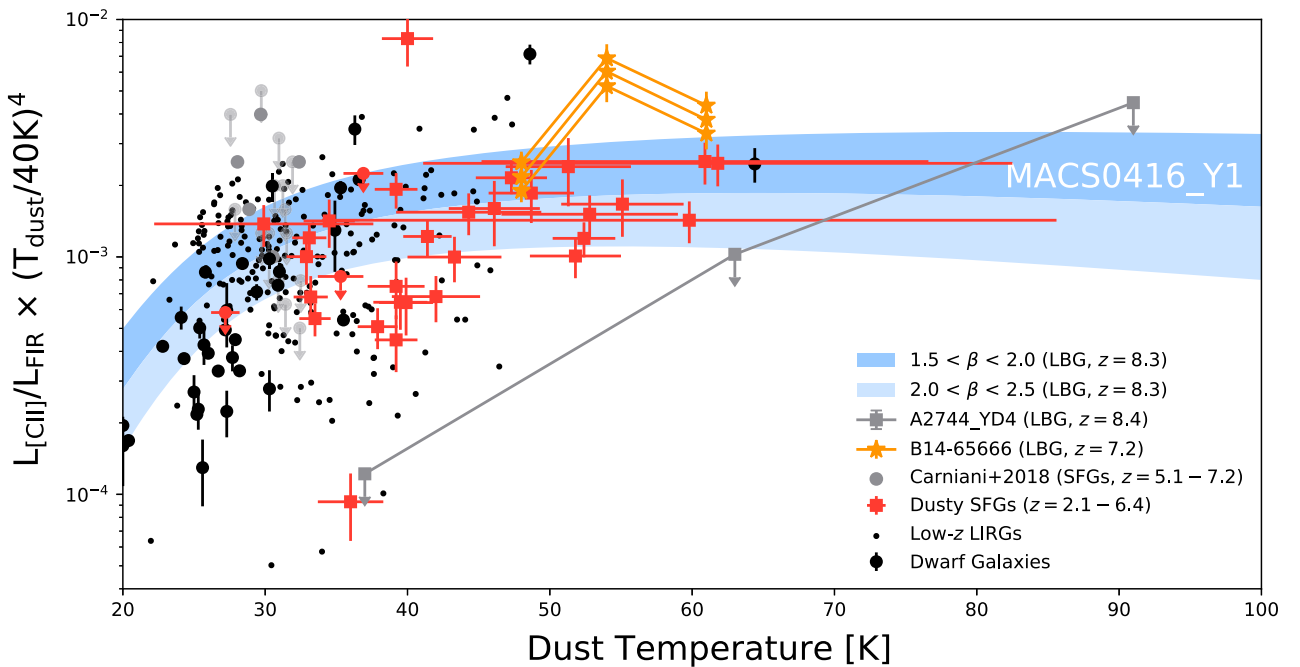


Figure 8. The temperature-corrected [C II] to FIR luminosity ratio is shown as a function of the dust temperature. We compare a range of temperatures and β s of MACS0416_Y1 against high-redshift LBGs, high-redshift DSFGs, low-redshift galaxies, and nearby dwarf galaxies. MACS0416_Y1 appears to have a similar ratio as the other sources, regardless of the dust temperature, and the ratio is only mildly dependent on β .

We compare our single-temperature fit of MACS0416_Y1 to high- and low-redshift sources. The temperatures of all the high-redshift galaxies are derived from either one or two wavelength observations. Hashimoto et al. (2019) provide the luminosity for three different β and temperature values ($[T_{\text{dust}}, \beta] = [48 \text{ K}, 2.0], [54 \text{ K}, 1.75], \text{ and } [61 \text{ K}, 1.5]$) for the entire source B14-65666 ($z = 7.15$ LBG), and for the two separate components. The upper-limit on [C II] emission of A2744_YD4 ($z = 8.38$ LBG) is shown for three different temperatures, since modelling by Behrens et al. (2018) suggests a significantly higher dust temperature (93 K) than the initial observations of Laporte et al. (2017) indicate (37–63 K). Furthermore, an ALMA Band-5 upper limit (Laporte et al. 2019) suggests a 3σ dust temperature lower limit of 43 K. Carniani et al. (2018) report the dust temperature, FIR luminosity, and [C II] emission of five sources (and 16 upper limits) at $z = 5\text{--}7$. The

luminosity was calculated for a 30 K, $\beta = 1.5$ single-temperature modified blackbody, although for graphing purposes we plot them with temperatures ranging from 25 to 35 K. Whilst the temperature in their analysis is fixed, the temperature-corrected luminosity ratio is similar across the temperature range, given the flatness of the blue fill, especially for higher temperatures. We show several dusty star-forming galaxies (DSFGs) at $2.1 < z < 6.4$. These consist of 20 sources detected with the South Pole Telescope (SPT), and 14 other DSFGs selected from various sub-mm/mm surveys (Gullberg et al. 2015). The low-redshift luminous infrared galaxies (LIRGs) are from the Great Observatories All-Sky LIRG Survey sample (Armus et al. 2009; Díaz-Santos et al. 2013), where we calculate the temperature using equation (2) in Díaz-Santos et al. (2017). The dwarf galaxies are from the Herschel Dwarf Galaxy Survey (Madden et al. 2013; Cormier et al. 2015).

We find a good agreement between the temperature-corrected [C II]-to-FIR luminosity ratio for MACS0416_Y1 compared to other sources over a large range of potential dust temperatures. Our agreement with the previously observed data does not depend on β , as adjusting the β from 1.5 to 2.5 only changes the luminosity ratio by a factor of ~ 3 . The graph further shows that the non-detection of A2744_YD4 (Laporte et al. 2019) does not appear to require a significantly lower [C II] luminosity than expected, especially when the temperature would be greater than 60 K, as a simulation in Behrens et al. (2018) indicated.

4.3.3 High β or high dust temperature?

Table 3 suggests either a high dust emissivity index ($\beta > 2$) or dust temperature ($T > 80$ K). Typical ULIRGs appear to have $\beta < 2$ (Clements et al. 2018), and the Milky Way has an average β around 1.6 (Planck Collaboration XI 2014). Similarly, only a few of the galaxies in Fig. 8 have dust temperatures beyond 50 K, and temperatures beyond 70 K appear out of the ordinary for anything but the recent simulation by Behrens et al. (2018, e.g. Faisst et al. 2017).

The high-redshift nature of MACS0416_Y1 will almost certainly result in a different chemical composition of the ISM due to the restricted number of elemental pathways for nucleosynthesis, when compared to low-redshift galaxies that allow for pathways that require more time, such as lower mass stars (e.g. Maiolino & Mannucci 2019). A different composition of dust grains could have caused a high β in MACS0416_Y1. For example, Demyk et al. (2013) find dust grain β values ranging from 0.8 to 3, depending strongly on the specific chemical composition of the dust grains. They provide an overview of the physics of dust emission, studied both with theoretical models and in laboratory experiments. Furthermore, the dust has to, almost exclusively, rely on SNe for its origin. At $z = 8.3$, the first stars have only been around for 500 Myr (Tegmark et al. 1997), so the time for $0.6 - 8 M_{\odot}$ stars to reach their AGB phase is restricted (> 100 Myr), and dust accretion growth is hindered by photo-ionization, the low metallicity, and the restricted time.

MACS0416_Y1 would not be the first observed galaxy with a $\beta > 2$. For example, ALMA observations by Kato et al. (2018) indicate a $\beta = 2.3 \pm 0.2$ in a Ly- α blob at $z = 3.1$. They suggest their high β is due to the chemical composition (Demyk et al. 2013). In the local Universe, Smith et al. (2012) find a high β (~ 3) in the galaxy core of Andromeda, and discusses its origin due to grain coagulation or icy mantles on the surface of grains in denser regions.

The dust produced in the initial episode of star formation in MACS0416_Y1, at around $z \sim 15$ (Tamura et al. 2019), could have been formed by Population III stars (Nozawa et al. 2014). De Rossi et al. (2018) suggest that this interstellar dust created by Population III stars would be silicate-rich, and the resulting FIR spectrum would appear substantially warmer than expected. They are able to match their predicted SED to Haro 11, a local, moderately low-metallicity galaxy ($\sim 0.25 Z_{\odot}$) undergoing a very young and vigorous starburst. These conditions suggest this galaxy approximates the relevant conditions for young Population III stars at high redshift. The existence of Population III stars has not been directly confirmed, however, and still remain controversial (e.g. Sobral et al. 2015, 2019; Bowler et al. 2017; Shibuya et al. 2018).

Of course, our observations of MACS0416_Y1 can only probe the dust that emits light, and therefore they probe the luminosity-weighted dust temperature (Scoville et al. 2016). Modelling by

Behrens et al. (2018) showed that this might significantly differ from the mass-weighted dust temperature distribution, especially for high-redshift sources. For the $z = 8.38$ source A2744_YD4, they find the hot dust to be mostly situated around compact young stellar clusters, whose strong interstellar radiation fields heat the dust efficiently due to the small optical depth. In their case, only 25 per cent of the dust is at $T_{\text{dust}} > 60$ K, but it contributes to more than 80 per cent of the luminosity. Thus, perhaps we are only witnessing a small portion of the dust that is exceptionally warm, with the majority of the dust existing at lower temperatures.

The size of the dust grains could further impact the dust temperature we see for MACS0416_Y1. Since dust growth is potentially suppressed by photo-ionization and does not have the time to coagulate in the early Universe, dust grain sizes of high-redshift galaxies might be smaller than in the local Universe. Ferrara et al. (2017) find that the grain size could change the temperature of the dust, with an increase in average dust temperature from 45 K for grains $> 0.1 \mu\text{m}$ to 60 K for grains smaller than $0.1 \mu\text{m}$.

Computer models are also suggesting that the high dust temperatures in MACS0416_Y1 are not an anomaly. Simulations by Arata et al. (2019) also find that dust temperatures of $z \sim 6$ galaxies could increase to ~ 70 K, and that the star-forming central region of their simulated galaxy appears to have the hottest dust. Their analysis shows a time-variable FIR luminosity, and with it the temperature. Due to stellar feedback processes, the simulated galaxy oscillates between a dust-obscured star-forming galaxy and UV-dominated galaxy with a reduced SFR. They also report on the difference between the mass- and luminosity-weighted dust temperature, and find a similar result as Behrens et al. (2018). The analytical model of primordial dust emission from De Rossi & Bromm (2019) also finds the central region to become brighter, relative to the total luminosity, for higher redshift galaxies. High-redshift systems are more concentrated (i.e. higher dust densities in the centre), enhancing the heating efficiency by stellar radiation, and increasing the luminosity-weighted temperature.

Finally, the high temperature in MACS0416_Y1 agrees with the high [O III]-to-[C II] ratio we find, as well as the relatively low metallicity ($\sim 0.2 Z_{\odot}$) inside this galaxy. The correlation between dust temperature and [O III]-to-[C II] ratio was also seen in observations by Díaz-Santos et al. (2017) and Walter et al. (2018), who show a correlation between this ratio and the dust temperature at both low and high redshifts. Faisst et al. (2017) find an anticorrelation between the metallicity and dust temperature, by studying a selection of lower redshift analogues of $z > 5$ galaxies with low metallicity. This might not be a fair comparison, since (i) the dust temperatures of these sources do not exceed 60 K, (ii) the most significant high-redshift source in Walter et al. (2018) is a quasar, which could potentially influence the heating mechanisms and the origin of the [O III] emission, and (iii) the [O III]-to-[C II] ratios of all sources in these studies range from 0.05 to 2.

4.3.4 Astronomical consequences

Our investigations of MACS0416_Y1 have only targeted the 90 and $160 \mu\text{m}$ rest-frame emission, as the [O III] $88 \mu\text{m}$ and [C II] $158 \mu\text{m}$ spectral lines are the only available bright lines visible in the atmospheric windows. Due to the long integration times required to detect MACS0416_Y1 and other high-redshift sources, most studies present an FIR luminosity with a single assumed temperature (e.g. Watson et al. 2015; Carniani et al. 2017). The luminosity varies significantly as a function of temperature, which not only poses

a problem for the analysis in the previous section, but also for astronomical studies in general.

One of the main conclusions from Tamura et al. (2019) is the existence of an older stellar population in MACS0416_Y1, determined using a dust evolution model to explain its dust mass and metallicity. The increase in dust temperature, combined with the potential change in β , can increase the per-mass luminosity of dust by 100-fold, as can be seen in Table 3, allowing the dust temperature to significantly impact the study of high-redshift objects in general. Moreover, the amount of dust seen in MACS0416_Y1 and other high-redshift galaxies (e.g. Hashimoto et al. 2019; Laporte et al. 2019) suggests an extreme dust-production scenario, where SNe have to produce dust at their maximum observed efficiency to reproduce the previously observed dust masses (Leśniewska & Michałowski 2019). The increase in dust temperatures reduces the required dust masses, and significantly relaxes the constraints on the dust production mechanisms at high redshift.

For MACS0416_Y1 in particular, the decrease in dust mass is not expected to significantly influence the age of the older stellar component (~ 300 Myr). While both the high metallicity and high dust mass of MACS0416_Y1 seemed to require a high age (Tamura et al. 2019), lowering the dust mass would still leave an intact metallicity-based lower limit on the age. However, determining the effects of a decrease in dust temperature on the older stellar population requires extensive modelling using stellar population synthesis models and dust production mechanisms, which is beyond the scope of this paper.

The reduction of dust mass in MACS0416_Y1 and other high-redshift galaxies due to increasing dust temperatures and/or β , however, does not mean that the dust-obscured star formation becomes less important. Arguably, it becomes more important, as the dust spectrum would peak at shorter wavelengths ($\lambda_{\text{peak}} \approx 40\text{--}70 \mu\text{m}$), which still remain largely unprobed in the high-redshift Universe, both due to the lack of sensitive instrumentation (as well as atmospheric opacity) in this wavelength range, and the lack of bright spectral lines in this wavelength range (although [O III] at $52 \mu\text{m}$ and [O I] at $63 \mu\text{m}$ are available). These spectral lines are often the main observational goal, where the dust continuum detection occurs almost serendipitously. We therefore advise towards a more thorough examination of dust temperatures in the early Universe, as well as the need for future instrumentation that can probe the peak of warm dust in the Epoch of Reionization, such as the planned Origins Space Telescope⁶ mission (Meixner et al. 2019).

5 CONCLUSIONS

We have detected the [C II] emission of an LBG at $z = 8.3116$, and provide a stringent upper limit on the 1.5 mm continuum emission. The [C II] emission compared to [O III] emission indicates strong interstellar radiation fields and/or a low PDR covering fraction, which is also seen for nearby dwarf galaxies with high [O III]-to-[C II] ratios. A spatial offset between the [C II] and [O III] emission suggests that the emission originates from a different part of the ISM. The [C II] emission traces the previously detected $850 \mu\text{m}$ dust continuum, suggesting it originates from the same ISM. The FIR to [C II] luminosity ratio is in line with previously found ratios for SMGs, suggesting a normal dusty ISM, when corrected for dust temperature. The velocity gradient across MACS0416_Y1 suggests it is a rotationally dominated, with a low stellar-to-dynamical gas

mass ratio, although we also discuss the potential of an outflow or inflow of gas.

No dust-continuum was detected at 1.5 mm down to $18 \mu\text{Jy}$ (3σ). Combined with the $137 \mu\text{Jy}$ dust continuum at $850 \mu\text{m}$, this indicates a significantly warmer dust component than local or mid-redshift galaxies, and would also necessitate a very high value of dust emissivity index (β) of 2, or potentially higher. We further discuss the risks of basing an FIR luminosity on one or two continuum measurements, and advise towards probing the short-wavelength part of the dust continuum.

ACKNOWLEDGEMENTS

This paper makes use of the following ALMA data: ADS/JAO.ALMA 2017.1.00225.S, 2016.1.00117, and 2013.1.00999.S. ALMA is a partnership of ESO (representing its member states), NSF (USA), and NINS (Japan), together with NRC (Canada), MOST and ASIAA (Taiwan), and KASI (Republic of Korea), in cooperation with the Republic of Chile. The Joint ALMA Observatory is operated by ESO, AUI/NRAO, and NAOJ. We would like to thank Nicholas Laporte for his insightful comments. TB and YT acknowledge funding from NAOJ ALMA Scientific Research grant no. 2018-09B and JSPS KAKENHI no. 17H06130. EZ acknowledges funding from the Swedish National Space Board. TO is financially supported by MEXT KAKENHI grant (18H04333) and the Grant-in-Aid (19H01931). TH was supported by Leading Initiative for Excellent Young Researchers, MEXT, Japan.

REFERENCES

- Appleton P. N. et al., 2013, *ApJ*, 777, 66
 Arata S., Yajima H., Nagamine K., Li Y., Khochfar S., 2019, *MNRAS*, 488, 2629
 Arata S., Yajima H., Nagamine K., Abe M., Khochfar S., 2020, preprint ([arXiv:eprint](https://arxiv.org/abs/2008.00000))
 Armus L. et al., 2009, *PASP*, 121, 559
 Asano R. S., Takeuchi T. T., Hirashita H., Inoue A. K., 2013, *Earth Planets Space*, 65, 213
 Avni Y., 1976, *ApJ*, 210, 642
 Barisic I. et al., 2017, *ApJ*, 845, 41
 Behrens C., Pallottini A., Ferrara A., Gallerani S., Vallini L., 2018, *MNRAS*, 477, 552
 Belitsky V. et al., 2018, *A&A*, 611, A98
 Binney J., Tremaine S., 2008, *Galactic Dynamics*, 2nd edn, Section on velocity profile.
 Bouwens R. J. et al., 2015, *ApJ*, 803, 34
 Bouwens R. J. et al., 2016, *ApJ*, 833, 72
 Bowler R. A. A., McLure R. J., Dunlop J. S., McLeod D. J., Stanway E. R., Eldridge J. J., Jarvis M. J., 2017, *MNRAS*, 469, 448
 Bradač M. et al., 2017, *ApJ*, 836, L2
 Capak P. L. et al., 2015, *Nature*, 522, 455
 Carilli C. L., Walter F., 2013, *ARA&A*, 51, 105
 Carniani S. et al., 2017, *A&A*, 605, A42
 Carniani S. et al., 2018, *MNRAS*, 478, 1170
 Castellano M. et al., 2016, *A&A*, 590, A31
 Ceccarelli C., Viti S., Balucani N., Taquet V., 2018, *MNRAS*, 476, 1371
 Chabrier G., 2003, *PASP*, 115, 763
 Clements D. L. et al., 2018, *MNRAS*, 475, 2097
 Cormier D. et al., 2015, *A&A*, 578, A53
 Cormier D. et al., 2019, *A&A*, 626, A23
 Cousin M., Guillard P., Lehnert M. D., 2019, *A&A*, 627, A131
 da Cunha E. et al., 2013, *ApJ*, 766, 13
 Dayal P., Ferrara A., 2018, *Phys. Rep.*, 780, 1
 de Looze I. et al., 2014, *A&A*, 568, A62

⁶<https://asd.gsfc.nasa.gov/firs/>

- De Rossi M. E., Bromm V., 2019, *ApJ*, 883, 113
- De Rossi M. E., Rieke G. H., Shivaeei I., Bromm V., Lyu J., 2018, *ApJ*, 869, 4
- Demyk K. et al., 2013, in *Proc. Life Cycle of Dust in the Universe: Observations*, p. 44
- Díaz-Santos T. et al., 2013, *ApJ*, 774, 68
- Díaz-Santos T. et al., 2017, *ApJ*, 846, 32
- Draine B. T., 2003, *ApJ*, 598, 1017
- Dunlop J. S. et al., 2017, *MNRAS*, 466, 861
- Dunne L., Eales S. A., 2001, *MNRAS*, 327, 697
- Erb D. K., Steidel C. C., Shapley A. E., Pettini M., Reddy N. A., Adelberger K. L., 2006, *ApJ*, 647, 128
- Faisst A. L. et al., 2017, *ApJ*, 847, 21
- Ferland G. J. et al., 2017, *RMxAA*, 53, 385
- Ferrara A., Viti S., Ceccarelli C., 2016, *MNRAS*, 463, L112
- Ferrara A., Hirashita H., Ouchi M., Fujimoto S., 2017, *MNRAS*, 471, 5018
- Ferrara A., Vallini L., Pallottini A., Gallerani S., Carniani S., Kohandel M., Decataldo D., Behrens C., 2019, *MNRAS*, 489, 1
- Finkelstein S. L. et al., 2015, *ApJ*, 810, 71
- Förster Schreiber N. M. et al., 2009, *ApJ*, 706, 1364
- Fujimoto S. et al., 2019, *ApJ*, 887, 107
- Gall C. et al., 2014, *Nature*, 511, 326
- Ginolfi M. et al., 2020, *A&A*, 633, A90
- Gnerucci A. et al., 2011, *A&A*, 528, A88
- González-López J. et al., 2017a, *A&A*, 597, A41
- González-López J. et al., 2017b, *A&A*, 597, A41
- Gullberg B. et al., 2015, *MNRAS*, 449, 2883
- Harikane Y. et al., 2019, preprint ([arXiv:1910.10927](https://arxiv.org/abs/1910.10927))
- Hashimoto T. et al., 2018, *Nature*, 557, 392
- Hashimoto T. et al., 2019, *PASJ*, 71, 71
- Infante L. et al., 2015, *ApJ*, 815, 18
- Inoue A. K. et al., 2016, *Science*, 352, 1559
- Jones G. C., Willott C. J., Carilli C. L., Ferrara A., Wang R., Wagg J., 2017, *ApJ*, 845, 175
- Kanekar N., Wagg J., Chary R. R., Carilli C. L., 2013, *ApJ*, 771, L20
- Kato Y. et al., 2018, *PASJ*, 70, L6
- Katz H. et al., 2019, *MNRAS*, 487, 5902
- Kawamata R., Oguri M., Ishigaki M., Shimasaku K., Ouchi M., 2016, *ApJ*, 819, 114
- Knudsen K. K., Richard J., Kneib J.-P., Jauzac M., Clément B., Drouart G., Egami E., Lindroos L., 2016, *MNRAS*, 462, L6
- Kohandel M., Pallottini A., Ferrara A., Zanella A., Behrens C., Carniani S., Gallerani S., Vallini L., 2019, *MNRAS*, 487, 3007
- Lagache G., Cousin M., Chatzikos M., 2018, *A&A*, 609, A130
- Laporte N. et al., 2015, *A&A*, 575, A92
- Laporte N. et al., 2016, *ApJ*, 820, 98
- Laporte N. et al., 2017, *ApJ*, 837, L21
- Laporte N. et al., 2019, *MNRAS*, 487, L81
- Leśniewska A., Michałowski M. J., 2019, *A&A*, 624, L13
- Lotz J. M. et al., 2017, *ApJ*, 837, 97
- Madau P., Dickinson M., 2014, *ARA&A*, 52, 415
- Madden S. C., Poglitsch A., Geis N., Stacey G. J., Townes C. H., 1997, *ApJ*, 483, 200
- Madden S. C. et al., 2013, *PASP*, 125, 600
- Magdis G. E. et al., 2011, *ApJ*, 740, L15
- Maiolino R., Mannucci F., 2019, *A&AR*, 27, 3
- Malhotra S. et al., 1997, *ApJ*, 491, L27
- Marrone D. P. et al., 2018, *Nature*, 553, 51
- Matthee J. et al., 2017, *ApJ*, 851, 145
- Mawatari K., Yamada T., Fazio G. G., Huang J.-S., Ashby M. L. N., 2016, *PASJ*, 68, 46
- Mawatari K. et al., 2020, *ApJ*, 889, 137
- McLeod D. J., McLure R. J., Dunlop J. S., Robertson B. E., Ellis R. S., Targett T. A., 2015, *MNRAS*, 450, 3032
- McMullin J. P., Waters B. P., Schiebel D., Young W., Golap K., 2007, in *Shaw R. A., Hill F., Bell D. J., eds, ASP Conf. Ser. Vol. 376, Astronomical Data Analysis Software and Systems XVI*. Astron. Soc. Pac., San Francisco, p. 127
- Meijerink R., Spaans M., Israel F. P., 2007, *A&A*, 461, 793
- Meixner M. et al., 2019, preprint ([arXiv:1912.06213](https://arxiv.org/abs/1912.06213))
- Michałowski M. J., 2015, *A&A*, 577, A80
- Nozawa T., Yoon S.-C., Maeda K., Kozasa T., Nomoto K., Langer N., 2014, *ApJ*, 787, L17
- Oesch P. A. et al., 2016, *ApJ*, 819, 129
- Oesch P. A., Bouwens R. J., Illingworth G. D., Labbé I., Stefanon M., 2018, *ApJ*, 855, 105
- Ota K. et al., 2014, *ApJ*, 792, 34
- Pallottini A., Ferrara A., Gallerani S., Vallini L., Maiolino R., Salvadori S., 2017a, *MNRAS*, 465, 2540
- Pallottini A., Ferrara A., Bovino S., Vallini L., Gallerani S., Maiolino R., Salvadori S., 2017b, *MNRAS*, 471, 4128
- Pallottini A. et al., 2019, *MNRAS*, 487, 1689
- Planck Collaboration XI, 2014, *A&A*, 571, A11
- Planck Collaboration XVI, 2016, *A&A*, 594, A13
- Planck Collaboration VI, 2018, preprint ([arXiv:1807.06209](https://arxiv.org/abs/1807.06209))
- Sawicki M., 2012, *PASP*, 124, 1208
- Schaerer D., Boone F., Zamojski M., Staguhn J., Dessauges-Zavadsky M., Finkelstein S., Combes F., 2015, *A&A*, 574, A19
- Scoville N. et al., 2016, *ApJ*, 820, 83
- Shibuya T. et al., 2018, *PASJ*, 70, S15
- Smit R. et al., 2018, *Nature*, 553, 178
- Smith M. W. L. et al., 2012, *ApJ*, 756, 40
- Sobral D., Matthee J., Darvish B., Schaerer D., Mobasher B., Röttgering H. J. A., Santos S., Hemmati S., 2015, *ApJ*, 808, 139
- Sobral D. et al., 2019, *MNRAS*, 482, 2422
- Solomon P. M., Vanden Bout P. A., 2005, *ARA&A*, 43, 677
- Stacey G. J., 2011, *IEEE Trans. Terahertz Sci. Technol.*, 1, 241
- Stacey G. J., Geis N., Genzel R., Lugten J. B., Poglitsch A., Sternberg A., Townes C. H., 1991, *ApJ*, 373, 423
- Stacey G. J., Hailey-Dunsheath S., Ferkinhoff C., Nikola T., Parshley S. C., Benford D. J., Staguhn J. G., Fiolet N., 2010, *ApJ*, 724, 957
- Tamura Y. et al., 2019, *ApJ*, 874, 27
- Tegmark M., Silk J., Rees M. J., Blanchard A., Abel T., Palla F., 1997, *ApJ*, 474, 1
- Vallini L., Ferrara A., Pallottini A., Gallerani S., 2017, *MNRAS*, 467, 1300
- Walter F. et al., 2018, *ApJ*, 869, L22
- Watson D., Christensen L., Knudsen K. K., Richard J., Gallazzi A., Michałowski M. J., 2015, *Nature*, 519, 327
- Willott C. J., Carilli C. L., Wagg J., Wang R., 2015, *ApJ*, 807, 180

¹*Division of Particle and Astrophysical Science, Graduate School of Science, Nagoya University, Aichi 464-8602, Japan*

²*National Astronomical Observatory of Japan, 2-21-1, Osawa, Mitaka, Tokyo 181-8588, Japan*

³*Tomonaga Center for the History of the Universe (TCHoU), Faculty of Pure and Applied Sciences, University of Tsukuba, Tsukuba, Ibaraki 305-8571, Japan*

⁴*Department of Environmental Science and Technology, Faculty of Design Technology, Osaka Sangyo University, 3-1-1, Nakagaito, Daito, Osaka 574-8530, Japan*

⁵*Department of Physics, School of Advanced Science and Engineering, Faculty of Science and Engineering, Waseda University, 3-4-1 Okubo, Shinjuku, Tokyo 169-8555, Japan*

⁶*Waseda Research Institute for Science and Engineering, Faculty of Science and Engineering, Waseda University, 3-4-1 Okubo, Shinjuku, Tokyo 169-8555, Japan*

⁷*Max-Planck-Institut für Extraterrestrische Physik (MPE), Giessenbachstr., D-85748 Garching, Germany*

⁸*Institute for Cosmic Ray Research, The University of Tokyo, Kashiwa, Chiba 277-8582, Japan*

⁹*Kyoto University Research Administration Office, Yoshida-Honmachi, Sakyo-ku, Kyoto 606-8501, Japan*

¹⁰*The Open University of Japan, 2-11 Wakaba, Mihama-ku, Chiba 261-8586, Japan*

¹¹*RIKEN Cluster for Pioneering Research, 2-1 Hirosawa, Wako-shi, Saitama 351-0198, Japan*

¹²*Institute of Astronomy, Graduate School of Science, The University of Tokyo, 2-21-1, Osawa, Mitaka, Tokyo 181-0015, Japan*

¹³*Observational Astrophysics, Department of Physics and Astronomy, Uppsala University, Box 516, SE-751 20 Uppsala, Sweden*

¹⁴*Research Center for the Early Universe, Graduate School of Science, The University of Tokyo, Tokyo 113-0033, Japan*

¹⁵*Department of Astronomical Science, The Graduate University for Advanced Studies (SOKENDAI), 2-21-1, Osawa, Mitaka, Tokyo 181-8588, Japan*

¹⁶*Faculty of Science, Hokkaido University, N10 W8 Kita-ku, Sapporo 060-0810 Japan*

¹⁷*Kitami Institute of Technology, 165 Koen-cho, Kitami, Hokkaido 090-8507, Japan*

¹⁸*Department of Physics, Graduate School of Science, The University of Tokyo, Tokyo 113-0033, Japan*

¹⁹*Kavli Institute for the Physics and Mathematics of the Universe (WPI), Todai Institutes for Advanced Study, The University of Tokyo, Kashiwa, Chiba 277-8583, Japan*

This paper has been typeset from a $\text{\TeX}/\text{\LaTeX}$ file prepared by the author.